Check for updates

RESEARCH ARTICLE

ADVANCED OPTICAL MATERIALS
www.advopticalmat.de

Introducing Relatively Isolated In/Out-Gap Bands in Cs_2XCl_6 (X = Sn, Hf, Zr, Ti) via B-Site Substitution: A Route to Brighter Luminescence and Tunable Emission Wavelengths

Zhenren Gao, Xing Shen, Pengbo Lyu, Changfu Xu,* Dong Fan, and Lizhong Sun**

Both theoretical and experimental approaches are utilized to investigate the fluorescence mechanism of B-site substituted Cs_2XCl_6 (A_2BX_6-type perovskite, X = Sn, Hf, Zr, Ti), aiming to enhance the luminescence and tune the emission wavelengths. Using Te-monosubstituted Cs_2SnCl_6 as a model system, thecomputational discovery that the introduction of out-gap and in-gap bands by Te can significantly enhance its transition dipole moment is reported. This is further experimentally confirmed, showing a single emission peak resulting from the radiative transition between the out-gap and in-gap bands. The broadening of the emission peak is attributed to self-trapped exciton (STE), while additional absorption/excitation peaks arise from composition segregation. Additionally, the high-throughput first-principles calculations indicate that substituting B-sites of Cs_2XCl_6 with Se, Te, Po, As, Sb, and Bi may also significantly enhance their light emission with the introduced bands. Thus, fine-tuning the emission wavelengths by controlling the position of out-gap and in-gap bands through cation selection is proposed. Furthermore, tunable white-light emission is achieved with excellent color stability by adjusting the Te and Bi composition in co-substituted Cs_2SnCl_6 material. The findings highlight the potential of utilizing out-gap and in-gap bands to tune luminescence in this perovskite family for advanced device applications, including white-light-emitting diodes (WLEDs).

1. Introduction

In recent years, metal halide perovskites (MHPs), particularly lead halide perovskites, have emerged as promising candidates for advanced photovoltaic and optoelectronic applications due to their exceptional properties such as high absorption coefficients, tunable light emission wavelengths, and narrow-band emission.[1] However, the toxicity and stability issues associated with lead perovskites have hampered their large-scale application.[2] In order to address the toxicity concerns associated with lead perovskites, significant attention has been focused on the development of novel perovskite materials based on low or nontoxic elements such as Sn, Te, Ge, and Bi. These materials possess electronic properties similar to those based on lead and are also promising for optoelectronic and photovoltaic applications.[3] However, challenges remain for these lead-free perovskite materials. For instance, although tin perovskites are promising alternatives to lead perovskites due to their low toxicity and abundance, they suffer from relatively poor environmental stability.[4] Cs_2SnCl_6 is a unique vacancy-ordered perovskite variant[5] of tin perovskite, which has drawn significant interest along with its derivatives due to their exceptional stability in air and moisture.[6] Its exceptionally high stability arises from a combination of the high concentration of Sn^{4+} (which is more inert than Sn^{2+} in air) and relatively high decomposition enthalpy (1.37 eV) compared to other perovskites (−0.09–0.47 eV).[7] However, intrinsic Cs_2SnCl_6 perovskite is a non-luminescent material due to the parity-forbidden nature of its electronic transitions.[7a,8] Similarly, intrinsic Cs_2XCl_6 (X = Hf, Zr, Ti) materials are also typically non-luminescent or inefficient for the same reason.[9] However, extensive research has shown that these materials, when in nanocrystal form, can emit light through fluorescence, which is often attributed to the localized charges induced by prominent surface defects.[7a,10] In addition, as large band gap materials, these intrinsic materials may also emit light in response to high-energy radiation. For instance, Cs_2HfCl_6 nanocrystals exhibit a broadband blue emission in exposure to gamma-radiation, with self-trapped exciton (STE) in $[HfCl_6]^{2-}$ octahedrons considered as the source of emission. This observation further substantiates the potential of Cs_2HfCl_6 as a highly promising scintillator for gamma spectroscopy.[9a,d,10a,b,11] Nevertheless, the application of intrinsic MHPs in bulk form for optoelectronic and photovoltaic purposes remains challenging due to the inherent parity-forbidden nature of their electronic transitions.

Z. Gao, X. Shen, P. Lyu, C. Xu, L. Sun
Hunan Provincial Key Laboratory of Thin Film Materials and Devices,
School of Material Sciences and Engineering
Xiangtan University
Xiangtan 411105, P. R. China
E-mail: pengbo.lyu@xtu.edu.cn; xcf@xtu.edu.cn; lzsun@xtu.edu.cn

D. Fan
ICGM
Université Montpellier, CNRS, ENSCM
Montpellier 34293, France

The ORCID identification number(s) for the author(s) of this article can be found under https://doi.org/10.1002/adom.202300956

DOI: 10.1002/adom.202300956

To unlock the full potential of Cs_2XCl_6 perovskite materials in optoelectronics and related fields, researchers are actively engaged in exploring methods to modify their electronic structures and thus enhance their luminescence performance. Typical approaches include doping or substitution with foreign atoms or ions, as well as synthesizing mixed-cation and mixed-halide perovskites, in order to overcome their parity-forbidden characteristics in electronic transition. Recently, significant progress has been made in these aspects,[6a,d,e,7a,12] for example, Sb-, Bi-, and Te-doped Cs_2SnCl_6 materials have been found to exhibit broadband orange-red (602 nm),[6d] blue (455 nm),[7a] and yellow-green (580 nm)[6a] luminescence, respectively. The corresponding highest photoluminescence quantum yield (PLQY) of 37%, 78.9%, and 95.4% were demonstrated at the concentrations of 0.59% (Sb),[6d] 2.75% (Bi),[7a] and 11% (Te),[6a] respectively. Recently, Zhang et al.[12a] achieved dual-band-tunable white-light emission with a PLQY of 68.3% in Cs_2SnCl_6 with Bi^{3+}/Te^{4+} co-doping. While defect complexes and STEs are believed to be responsible for the observed luminescence and broadband in doped Cs_2SnCl_6, the exact mechanism is still an active area of research, and further exploration is needed to fully understand the luminous origin at the microscopic level.[6a,d,7a,13] Moreover, the precise control of light emission wavelength in perovskite materials is a significant research focus within the field.[14] The limited exploration of how B-site substitution affects the luminescence properties of the Cs_2XCl_6 material family emphasizes the importance of additional research. This investigation is essential for achieving effective control over the light emission wavelength in this particular group of perovskite materials.

In this study, we investigated the impact of B-site substitution on luminescence and the fluorescence mechanism in Cs_2XCl_6 materials, with a focus on Te-monosubstituted Cs_2SnCl_6 perovskite, using a combination of theoretical and experimental methods. Our first-principles calculations allowed us to understand the electronic origin of non-fluorescence or inefficient fluorescence in intrinsic Cs_2XCl_6 perovskite. Then we explored the effect of Te substitution on luminescence performance specifically in the model system Cs_2SnCl_6. Through our research, we conclusively showed that Te substitution induces the formation of in-gap bands and out-gap bands within the host energy bands. This leads to a substantial improvement in electronic transition probability and light emission. Our experimental findings solidify the fact that luminescence is significantly enhanced in Cs_2SnCl_6 samples with varying concentrations of Te substitution. The samples we synthesized displayed a single emission peak at ≈580 nm, which was confirmed to result from the radiative transition between out-gap bands and in-gap bands. The broadening of the emission peak is attributed to STE. In addition, we provided insight into fluorescence attenuation at high Te concentrations and revealed the resonance transfer of energy from the Cs_2SnCl_6 phase to nearby $Cs_2Sn_{1-y}Te_yCl_6$ phase, which enhances light emission due to the composition segregation[15] phenomenon. Subsequently, our analysis of $Cs_2X_{1-y}Y_yCl_6$ using high throughput first-principles calculations identified promising luminescent materials substituted with Se, Te, Po, As, Sb, and Bi. Our findings suggest that it is possible to achieve the desired emission wavelengths by appropriately selecting substituting cations, as the radiative transition between in-gap bands/out-gap bands can occur regardless of the host materials. Finally, we achieved tunable white-light emission with excellent color stability by adjusting the composition ratio of Te and Bi in Te and Bi co-substituted Cs_2SnCl_6 materials, showcasing the effectiveness of using in-gap bands/out-gap bands to control luminescence and laying the foundation for the development of high-performance perovskite-based optoelectronic devices. Overall, our study contributes to the understanding of the fluorescence mechanism in halide perovskites and provides new directions for the development of perovskite-based optoelectronics.

2. Results and Discussion

2.1. First-Principles Analysis of Intrinsic Cs_2XCl_6 (X = Sn, Hf, Zr, Ti)

The A_2BX_6-type[5a,16] tin halide perovskite Cs_2SnCl_6 belongs to the vacancy-ordered double halide perovskite[5] with space group *Fm-3m* (No. 225), as illustrated in Figure 1a and Figure S1 (Supporting Information). To understand the underlying mechanism of the non-fluorescence phenomenon observed experimentally in its bulk materials,[7a,8] we conducted density functional theory calculations at HSE06 level to obtain its electronic structure. The projected band structure (upper panel of Figure 1b) reveals that the energy bands near the conduction band minimum (CBM) are distributed in the energy window of 4.07–5.06 eV, originating from the antibonding states composed of Cl-*p* and Sn-*s* orbitals. Conversely, the energy band near the valance band maximum (VBM) contributed by Cl-*p* states is relatively localized. Although CBM- and VBM-associated partial charge densities (Figure 1c) exhibit symmetric distributions due to the highly symmetric structure characteristic of $[SnCl_6]^{2-}$ octahedron, there is little overlap between them. In addition, a gap of 2.57 eV exists between the 4th conduction band and the 5th conduction band. Therefore, the conduction bands near Fermi level are relatively isolated. Despite the favorable direct band gap (E_g = 4.07 eV) of Cs_2SnCl_6 perovskite for luminescence, our computational analysis reveals that its CBM and VBM have the same even-parity (Γ^+) at the Γ point as shown in the upper panel of Figure 1b, resulting in a parity-forbidden transition with zero-transition dipole moment. Moreover, the calculated transition dipole moment between the CBM band (band number 149) and the VBM band (band number 148) is overall very weak (lower panel of Figure 1b). It is important to notice that the effects of spin-orbit coupling (SOC) on electronic structure and transition dipole moment can be safely disregarded when considering both the HSE06 and PBE functionals. This assertion is substantiated by the findings depicted in Figure 1b,c and Figure S2 (Supporting Information), where it is evident that the band structures and transition dipole moment remain relatively stable when SOC is taken into account. Although SOC does affect the magnitude of transition dipole moment, the presence of analogous curves and the minimal difference in magnitude (>1.5 $Debye^2$) indicate that these disparities can be neglected. Particularly noteworthy, the discrepancy at the Γ point is zero. Therefore, the absence of luminescence in Cs_2SnCl_6 can be attributed to the parity-forbidden transition with a zero-transition dipole moment and the non-overlapping partial charge densities and wave functions of the CBM and VBM.[17] We observe a similar phenomenon in Cs_2XCl_6 (X = Hf, Zr, Ti), as demonstrated in Figures S3–S5 (Supporting Information). To enhance their

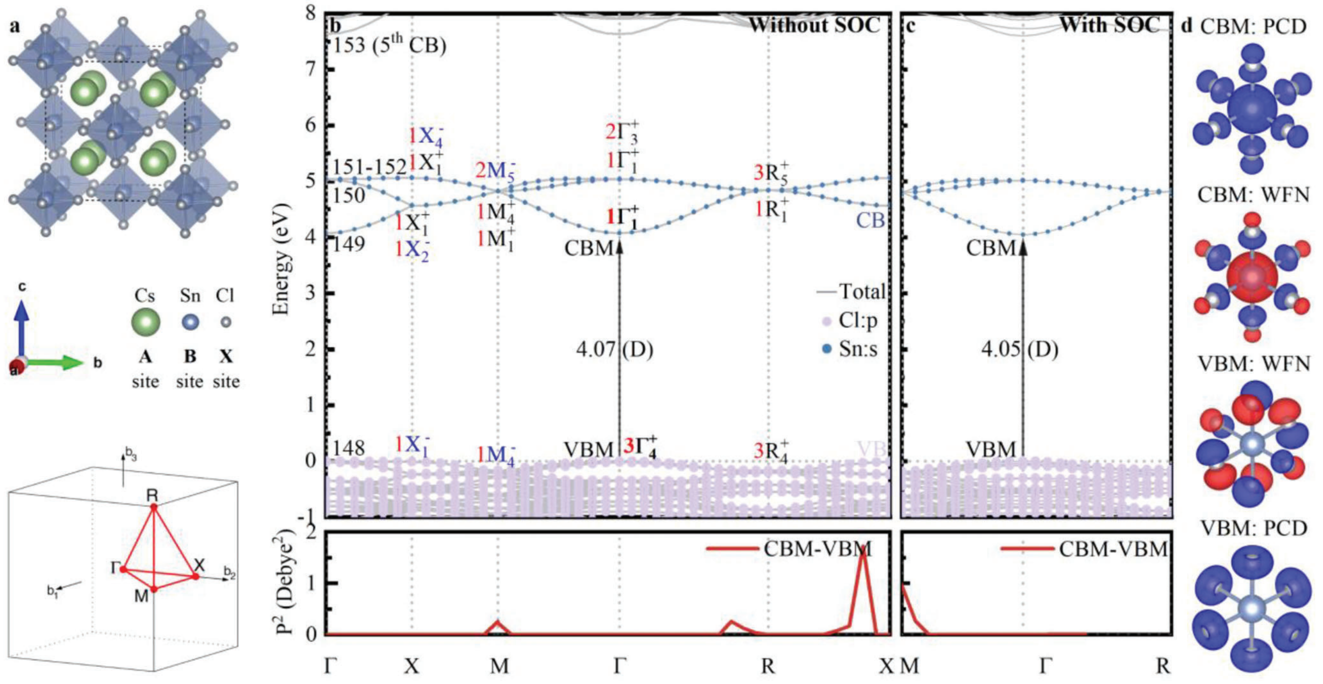

Figure 1. Crystal structure and electronic properties. a) Crystal structure of Cs_2SnCl_6 and its high symmetry points in Brillouin zone. b,c) Projected band structures (upper panels) with or without SOC and their transition dipole moments (lower panels), they are obtained from HSE06 functional. The black number next to the energy band represents the band number. The $3\Gamma^+{}_4$-like symbol is the Koster notation for irreducible representation, and the red number in front of it represents multiplicity. The symbols "-" and "+" represent odd and even parities, respectively. CB and VB represent conduction band and valence band, respectively. These definitions also apply to other similar graphs. d) CBM- and VBM-associated partial charge densities (PCDs) and wave functions (WFNs) without SOC, and only one octahedron is shown here for clarity.

photoelectric characteristics, we proceed to investigate the influence of B-site substitution on the electronic and luminescent properties of Cs_2XCl_6 (X = Sn, Hf, Zr, Ti) perovskites.

2.2. Luminescence Characterization of Te-Monosubstituted Cs_2SnCl_6

As a starting point, we chose Te-monosubstituted Cs_2SnCl_6 as a model system to investigate the changes in its electronic structure and luminescence performance following the substitution. To conduct our study, we employed first-principles calculations using a 36-atom unit cell of Cs_2SnCl_6 perovskite with Te substitution at the B-site. The results are summarized in **Figure 2**. The energy band structure of $Cs_2Sn_{0.75}Te_{0.25}Cl_6$ (Figure 2a) shows that the energy bands within the energy window of −1–−0.5 and 2–3 eV correspond to the intrinsic valence bands and conduction bands of the host Cs_2SnCl_6, respectively. With the substitution of Te, new impurity bands appear in the energy windows of −1–0 and 2.5–3.5 eV. The former bands are referred to as in-gap bands (IGBs) and are primarily composed of Cl-*p* and Te-*s* states. They are located between the intrinsic valence and conduction bands. The latter bands are defined as out-gap bands (OGBs) and are primarily composed of Cl-*p* and Te-*p* states. They are located in the intrinsic conduction bands. At lower Te contents, both in-gap and out-gap bands tend to develop into localized quasi-flat bands. However, as the Te content increases, the localization of these bands gradually diminishes, and their broadening expands (as illustrated in Figure 2b–d). This evolution sets them apart from the defect energy levels that emerge from doping. Typically, these defect levels arise from ultra-low concentration doping (<1%) and often manifest as non-dispersive, highly localized horizontal lines within the energy band. As the concentration of doping or substitution rises (>10%, as in this work), more doped or substituted atoms are introduced, augmenting the interactions between atoms. Consequently, the confinement of electrons within individual atoms wanes, and electrons begin to assume collective motion. This shared electron motion leads to the splitting of energy levels, resulting in the formation of numerous closely spaced, seemingly continuous energy levels—an occurrence that gives rise to energy bands. In contrast to energy levels, energy bands manifest as curves featuring a certain degree of dispersion and broadening. Conversely, as the Sn content decreases, the intrinsic conduction bands near Fermi level become increasingly localized, and their broadening decreases gradually. Eventually, the intrinsic conduction bands near Fermi level vanish entirely when Te fully substitutes Sn. It is worth noting that while the influence of SOC on the intrinsic bands might be negligible, its influence on the in-gap bands and out-gap bands introduced by the heavy atoms such as Te is substantial, as evidenced in Figure 2e–h.

Our research demonstrates that in-gap bands and out-gap bands have even- and odd-parity properties respectively at low Te concentration, which results in a significant transition dipole moment between them. However, as shown in Figure 2i–l, the transition dipole moment at the Γ point (i.e., the location of the

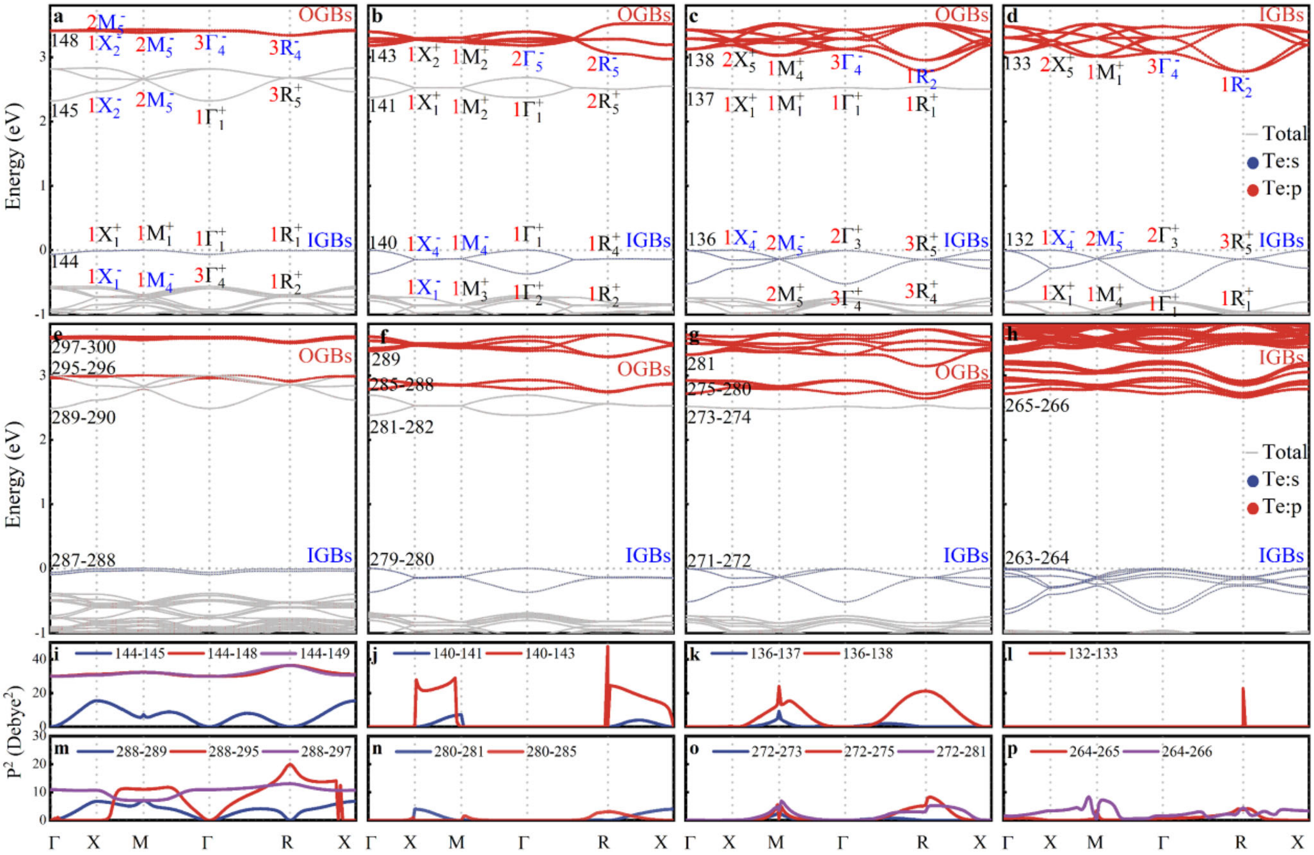

Figure 2. Electronic structure and transition dipole moment. a–d) Projected band structures and i–l) the corresponding transition dipole moments without SOC for $Cs_2Sn_{1-y}Te_yCl_6$ (y = 0.25, 0.50, 0.75, 1.00; from left to right). e–h) Projected band structures and m–p) the corresponding transition dipole moments with SOC for $Cs_2Sn_{1-y}Te_yCl_6$ (y = 0.25, 0.50, 0.75, 1.00; from left to right). The black number next to the energy band represents the band number. After considering SOC, the energy band undergoes splitting. For example, the original band 144 (Figure 2a) splits into bands 287 and 288 (Figure 2e), while the original band 148 (Figure 2a) splits into bands 295 and 296 (Figure 2e).

direct band gap) between in-gap bands and the intrinsic conduction bands near Fermi level can be disregarded across all concentrations. These observations indicate that the transition between in-gap bands and out-gap bands play a vital role in generation of yellow-green light emissions observed before,[6a,e,12a] rather than those parity-forbidden transitions such as in-gap bands to the intrinsic conduction bands near Fermi level (see Figure 2). The transition dipole moment between in-gap bands and out-gap bands reaches maximum at a Te concentration of 25%, but decreases as the Te concentration increases further, as depicted in the Figure 2i–l. Furthermore, the rise in Te content causes a shift from a direct to an indirect bandgap between in-gap bands and out-gap bands, impeding the electronic transition between these two bands. As illustrated in Figure 2i–p, SOC induces a reduction in the magnitude of transition dipole moment.

As a further stage, we conducted experimental research on Te-monosubstituted Cs_2SnCl_6 to explore the influence of in-gap bands and out-gap bands on the luminescence mechanism of the B-site monosubstituted Cs_2XCl_6 perovskite family. We synthesized a series of Cs-Sn-Te-Cl quaternary compounds with the formula $Cs_2Sn_{1-y}Te_yCl_6$ (y = 0.10, 0.30, 0.50, 0.70, 0.90, 1.00), using the solvothermal method.[12b] As shown in Figure 3a,b, the powder samples have amorphous geometry microstructures with particle sizes ranging from 5 to 50 µm. The structural characterization confirm that Sn and Te are distributed in every corner of the sample, which is consistent with previous research.[6a,12a] Importantly, the synthesized sample is determined to be a solid solution with composition segregation,[15] which consist of $Cs_2Sn_{1-y}Te_yCl_6$ phase and Cs_2SnCl_6 phase. Upon irradiation of an ultraviolet (UV) lamp (365 nm), the intrinsic Cs_2SnCl_6 perovskite does not show any luminescence, whereas significant yellow-green photoluminescence (PL) occurs upon Te substitution (lower panel, Figure 3c), which is consistent with previous studies.[6a,e,12a] More discussions are shown in Supplementary Information.

It should be noted that although double absorption/excitation peaks were observed (Figure S6, Supporting Information), only a single emission peak exists with a central emission wavelength of ≈580 nm (2.14 eV), a Stokes shift of ≈200 nm, and a full width at half-maximum (FWHM) exceeding 120 nm, as shown in Figure 3d. The center of the emission peak slightly redshifts from 580 to 590 nm as the Te content increases, while maintaining the same shape and FWHM. Although researchers have previously reported similar observations and proposed several potential explanations for the single emission peak,[6a,e,12a] their explanations are primarily based on systems with low-concentration doping which introducing impurity levels. According to our

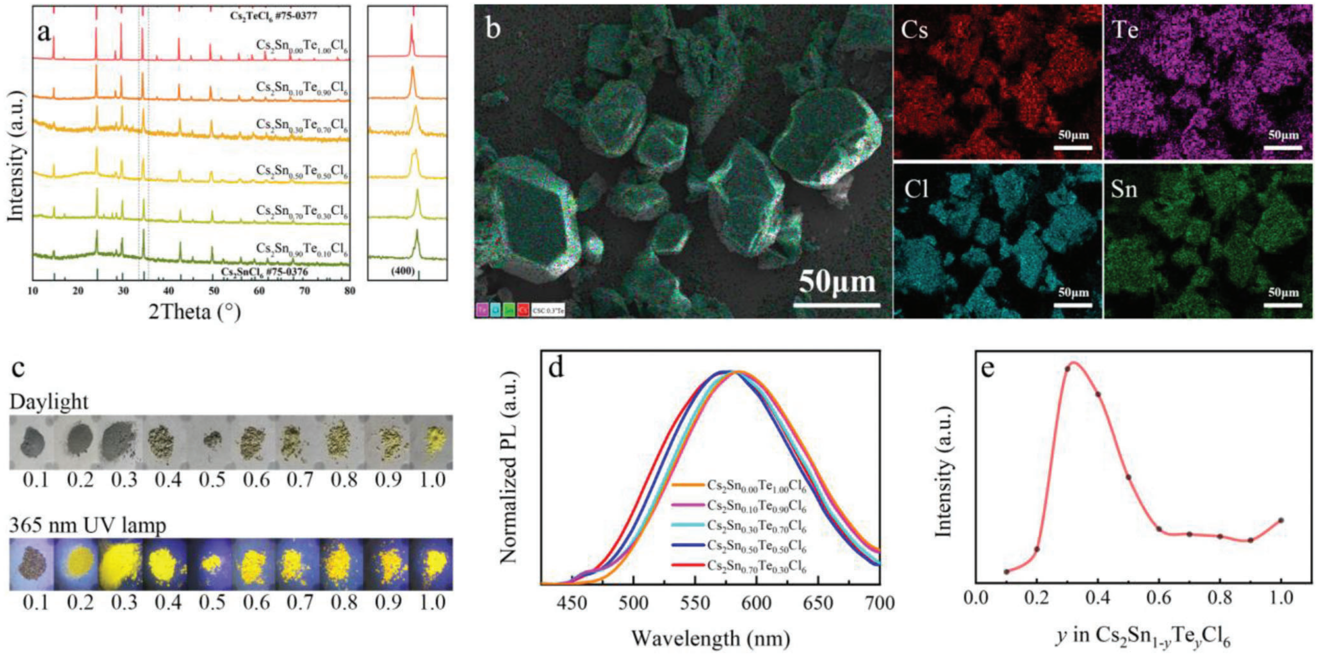

Figure 3. Structural characterization and luminescence properties. a) X-ray diffraction patterns of $Cs_2Sn_{1-y}Te_yCl_6$ ($y = 0.10, 0.30, 0.50, 0.70, 0.90, 1.00$), and the attached pattern shows the enlarged diffraction peaks near 34°. b) Scanning electron microscopy image of $Cs_2Sn_{0.70}Te_{0.30}Cl_6$ sample and its energy dispersive spectrometry elemental mappings. c). Photographs of $Cs_2Sn_{1-y}Te_yCl_6$ ($y = 0.10, 0.20, 0.30, 0.40, 0.50, 0.60, 0.70, 0.80, 0.90, 1.00$; from left to right) powders exposed to daylight (upper) and 365 nm UV lamp (lower). d) Normalized PL spectra. e) Change trend of PL spectrum peak with the Te content increasing.

first-principles calculations (see Figure 2), it becomes evident that elevated concentrations of Te lead to the emergence of impurity bands within the host bands, as elaborated upon in the initial paragraph of Section 2.2. Therefore, explanations based on low-concentration doping may not be applicable in our study. Notably, we observed that the compositional segregated Cs_2SnCl_6 phase is responsible for the appearance of additional excitation and absorption peaks, and further details are shown in Supporting Information. However, the exact electronic origin of the single emission peak remains unresolved and requires further investigation.

The fluorescence excitation and emission spectra, observed at different monitoring wavelengths (Figure S7, Supporting Information), exhibit similarities. This suggests that the emission band is an inherent characteristic of the sample. Hence, it can be inferred that the PL emission in these systems originates from the same radiative transition, irrespective of the excitation wavelength. However, the precise PL transition that accounts for the fluorescence emission needs to be located. By analyzing the lack of fluorescence observed in Cs_2SnCl_6, the significantly higher calculated transition dipole moment (Figures 1 and 2) between in-gap bands and out-gap bands than other transitions in Te-monosubstituted Cs_2SnCl_6, and the resemblance of the yellow-green emission between Cs_2TeCl_6 [18] and Te-monosubstituted Cs_2SnCl_6 materials, we can conclude that the single emission peak observed in the fluorescence spectrum of Te-monosubstituted Cs_2SnCl_6 arises from the transition between out-gap bands and in-gap bands introduced by Te substitution. Moreover, the intensity of fluorescence shows an initial increase and subsequent decrease as Te content increases. Notably, the $Cs_2Sn_{0.70}Te_{0.30}Cl_6$ sample exhibiting the highest fluorescence intensity, as illustrated in Figure 3e and Figure S8 (Supporting Information). This trend is consistent with the trend observed in the calculated transition dipole moment as shown in Figures 1 and 2. Therefore, the decrease in emission intensity at high concentrations of Te substitution can be attributed to the low transition dipole moment, in addition to the transition from a direct bandgap to an indirect bandgap between in-gap bands and out-gap bands, as shown in Figure 2. Our findings are further supported by the low PLQY of Cs_2TeCl_6 (corresponding to the electronic structure shown in Figure 2d) as reported by Jiang et al.[18]

After identifying the dominant radiative transition responsible for the luminescence, we delved deeper into the luminescence mechanism of Te-monosubstituted Cs_2SnCl_6. According to literature,[10a,c,d,f,19] luminescence of insulating halides is most often caused by localized charges such as polarons and excitons. However, it is worth noting that polarons are typically encountered in nanocrystalline materials,[10a,c,d,f] whereas their presence in large-size bulk materials is limited to a negligible extent, thereby allowing their exclusion from consideration in bulk materials. Therefore, the impact of polarons can be negligible in our work, since the samples we synthesized belong to large-size bulk materials. On the other hand, localized excitons, i.e., STE, have been commonly recognized as the main cause of radiative recombination in insulating halides, playing a pivotal role in understanding luminescence phenomena. To confirm if STE accounts for the luminescence in Te-monosubstituted Cs_2SnCl_6, we have conducted additional investigations combining experimental and computational approaches. The observed broadening of the single emission peak of Te-monosubstituted

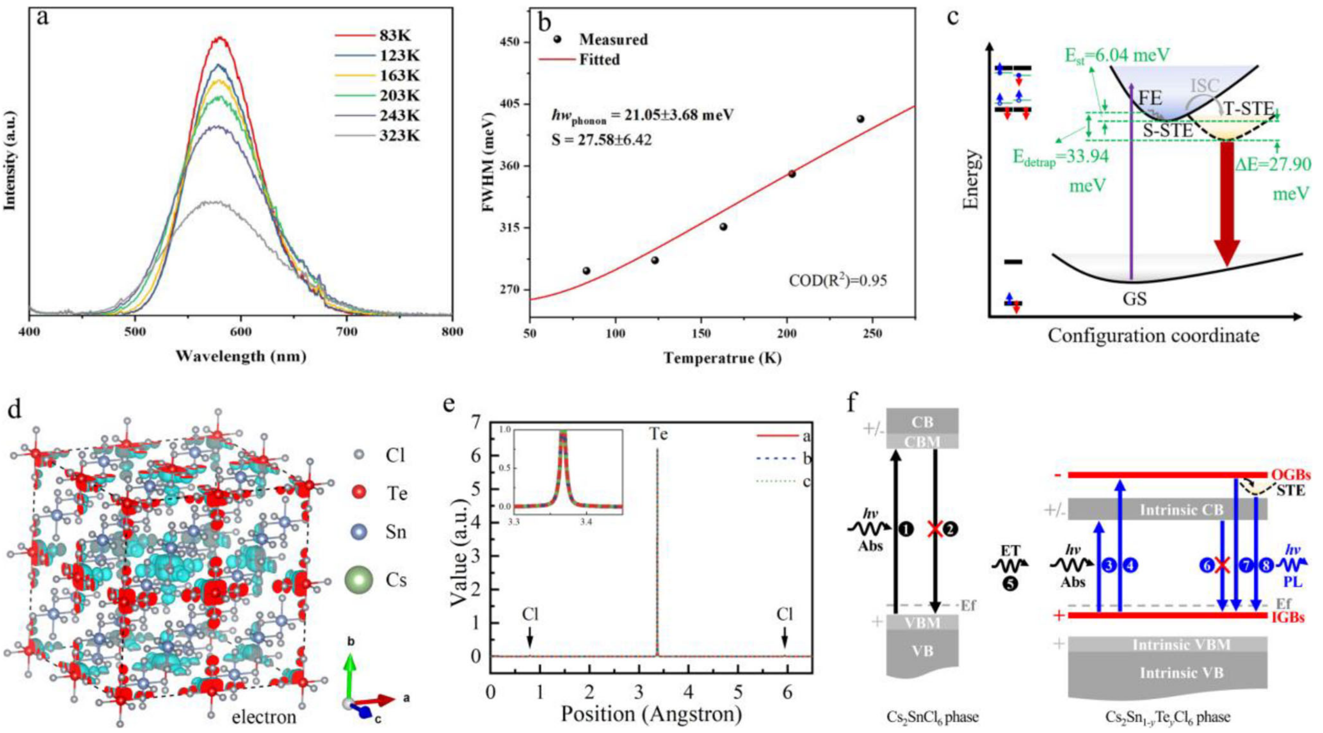

Figure 4. Temperature-dependent fluorescence spectra measurement, excited state calculation and luminescence mechanism. a) Temperature-dependent fluorescence spectra of $Cs_2Sn_{0.70}Te_{0.30}Cl_6$ sample. b) Fitting between the FWHM of emission peak and temperature. c) Configuration coordinate diagram. GS: ground state; FE: free exciton; S-STE: spin-singlet self-trapped exciton; T-STE: spin-triplet self-trapped exciton; ISC: intersystem crossing; RISC: reverse intersystem crossing; E_{st} (E_{trap}): self-trapping depth; E_{detrap}: detrapping barrier; ΔE: energy separation between T-STE and S-STE; The inset (lower left) shows the energy levels and their electronic states for GS; the insets (upper left) show the energy levels and their electronic states for excited states (spin singlet and spin triplet). d) Electron-associated partial charge densities in T-STE. e) Electron density distribution along the direction of Cl-Te-Cl in $[TeCl_6]^{2-}$ octahedron, note that the identical curves corresponding to the a, b, and c directions (insert) imply an isotropic distribution. f) Luminescence mechanism of Te-monosubstituted Cs_2SnCl_6 sample. The left panel represents the Cs_2SnCl_6 phase and the right panel represents the $Cs_2Sn_{1-y}Te_yCl_6$ phase. ET and Ef represent energy transfer and Fermi level, respectively.

Cs_2SnCl_6, with a 120 nm FWHM, served as the first evidence of STE mechanism, as proposed in previous report for other perovskite systems.[13,20] To further confirm it, we conducted temperature-dependent fluorescence spectra measurement on a typical sample $Cs_2Sn_{0.70}Te_{0.30}Cl_6$, because the strong electron-phonon coupling is prominent feature of STE emission.[21] As shown in Figure 4a,b, the fluorescence intensity increases gradually as the temperature decreases, indicating the suppression of phonon-related non-radiative transition processes. The temperature-dependent FWHM aligns well with the phonon broadening model, and the derived Huang-Rhys factor S of 27.58 (±6.42) suggests a significant level of electron-phonon coupling. Therefore, it is plausible that the STE has a key impact on the luminescence mechanism of Te-monosubstituted Cs_2SnCl_6. This is further supported by our excited states calculations using the DeltaSCF method. The computations are performed using a supercell containing 288 atoms, and the results are shown in Figure 4c,d. Based on our findings, we propose that upon illumination, the excited electron-hole pair forms free excitons (FE) under the influence of Coulomb interaction. Subsequently, FE self-traps into spin-singlet self-trapped exciton (S-STE) and further self-traps into more stable spin-triplet self-trapped exciton (T-STE) through spin flip and intersystem crossing. The energy separation (ΔE) is calculated as 27.90 meV between the T-STE and the S-STE, which is slightly higher than the thermal activation energy at room temperature (≈25 meV). The DeltaSCF method may not yield highly accurate outcomes as a compromise approach for computing excited states. Although a small difference of 2.90 meV cannot be excluded within the error bar of DeltaSCF, qualitative comparisons can often yield more meaningful insights when dealing with such compromises. Therefore, T-STE can be detrap from the T-STE state to the S-STE state through reverse intersystem crossing[22] at room temperature, indicating the existence of thermal equilibration between the two self-trapped excitons. Detrapping barrier (E_{detrap}) is the difference between the STE states and FE configurations in the excited state, which is considered the energy that the self-trapped electron-hole pair needs to overcome to become a free electron-hole pair (i.e., FE) that can move freely.[23] It can be obtained by the following equation:

$$E_{detrap} = E_S^{unrelax} - E_T^{relax} \tag{1}$$

where $E_S^{unrelax}$ is the total energy of the unrelaxed spin-singlet excited state (i.e., FE state), and E_T^{relax} is the total energy of the relaxed spin-triplet excited state. The detrapping barrier (E_{detap}) from the most stable spin-triplet self-trapped exciton to free exciton is actually 33.94 meV, which is comparable to that of 35 meV in (TDMP)$PbBr_4$,[23b] and 34 meV in $CsPbBr_3$,[24] both of which have demonstrated STE luminescence. The observed E_{detap} is higher than the thermal activation energy of 25 meV at room temperature, and the difference of ≈10 meV might indicate the coexistence and dynamic equilibrium between FE and STE. While a complete exclusion of STE detrapping might not be absolute, the STE state may be a significant population at room temperature, i.e., the excited electron-hole pairs have a tendency to undergo self-trapping. As reported by Tao et al.[24] and Gautier et al.,[23b] a higher detrapping barrier than the room thermal activation energy indicates that it is more favorable for the STE emission relatively to the FE emission. Furthermore, the partial charge densities associated with electrons and holes (as depicted in Figure 4d; Figure S13a, Supporting Information) within T-STE predominantly exhibit localization within the $[TeCl_6]^{2-}$ octahedron. Particularly noteworthy is the heightened electron/hole density localization on the Te atom, as evidenced by the calculated electron/hole density distribution along the Cl-Te-Cl direction within the $[TeCl_6]^{2-}$ octahedron (depicted in Figure 4e; Figure S13b, Supporting Information). This robustly suggests that excitons are likely to be trapped and localized specifically within the Te atom residing within the Te octahedron. The noteworthy distinction between E_{trap} (6.04 meV, representing the energy difference between FE and the relaxed spin-singlet excited state) and E_{detrap} (33.94 meV) serves as an indication that excitons have a propensity to take the form of T-STE, rather than T-STE undergoing dissociation into FE or free carriers.[23a]

2.3. First-Principles Analysis of B-Site monosubstituted Cs_2XCl_6 (X = Sn, Hf, Zr, Ti)

We have observed that the occurrence of in-gap bands and out-gap bands is not limited to Te-monosubstituted Cs_2SnCl_6, as demonstrated by their appearance in Bi-substituted Cs_2SnCl_6, as shown in Figure S14 (Supporting Information). We anticipate these bands can also be introduced into Cs_2XCl_6 materials via B-substitution. Therefore, it is possible to further enhance the luminescence and tune the emission wavelengths by varying the substituting cations. To this end, we performed additional first-principles calculations to investigate the electronic structures and luminescence performance of B-site substituted $Cs_2X_{1-y}Y_yCl_6$ (X = Sn, Hf, Zr, Ti; Y = Sn, Al, Ga, In, Tl, Ge, Se, Te, Po, As, Sb, Bi) at a concentration of 25%. The band structures, parity properties, transition dipole moments, and Gibbs free energy of additional substituted systems are presented in **Figure 5** and Figures S15–S63 (Supporting Information). Our analysis confirms the presence of in-gap bands only, out-gap bands only, or in-gap bands/out-gap bands concurrently in all of the tested systems. We also observed that the positions of these bands within the host energy bands differ depending on the introduced cations. We classify in-gap bands/out-gap bands into four types based on state composition (type **1** or **2**) in addition their positions (in-gap bands/out-gap bands). IGBs**1** and OGBs**1** are composed mainly of Cl-*p* and Y-*s* states, and have even-parity, which is the same as the intrinsic VBM band. In contrast, IGBs**2** and OGBs**2** are derived from the hybrid orbitals of Cl-*p* and Y-*p*, have odd-parity. It is worth noting that Cs_2XCl_6 (X = Sn, Zr, and Ti) materials with Te monosubstitution exhibit similar positions of in-gap bands and out-gap bands. Moreover, previous studies have reported that these materials display a comparable yellow-green PL ≈580 nm originating from the luminescent center $[TeCl_6]^{2-}$, irrespective of the hosting materials.[6a,e,12c,25] These findings support our conclusion that the fluorescence emission is closely linked to the presence of in-gap bands and out-gap bands, which depend on the substituting Y (in this case, Te) cation and are independent of the host materials. Other $Cs_2X_{0.75}Y_{0.25}Cl_6$ materials, were also analyzed and in-gap bands, out-gap bands, and the intrinsic conduction bands near Fermi level were identified. The intrinsic conduction bands near Fermi level were found to have a consistent position and broadening across different Y substitutions for the same X, indicating their insensitivity to the Y substituent. Similar trends were observed for both in-gap bands and out-gap bands in all these systems studied.

The $Cs_2X_{0.75}Y_{0.25}Cl_6$ series materials have been classified into three categories based on the effect of in-gap bands/out-gap bands on electronic transitions and light emission, depicted in **Figure 6**. Category I is characterized by the presence of only IGBs**1** or OGBs**1** located near the the intrinsic conduction bands. However, the impact of these IGBs**1** or **2** on electronic transitions is minimal, as they have the same parity as the intrinsic VBM, and the transitions from the intrinsic VBM to these bands are parity-forbidden. Materials that fall under this category include $Cs_2Sn_{0.75}Y_{0.25}Cl_6$ (Y = Ga, In, Tl, Ge) materials, among others. Category II is distinguished by the simultaneous presence of even-parity IGBs**1** and odd-parity OGBs**2**/IGBs**2**, which play a crucial role in electronic transitions. This is because the combination of IGBs**1** and OGBs**2** with opposite parity can overcome the parity-forbidden selection rule, contributing to a significant increase in the transition dipole moment and consequent enhancement of light emission. This category includes materials such as $Cs_2Sn_{0.75}Y_{0.25}Cl_6$, where Y can be Se, Te, or Po, as well as other Cs_2XCl_6 systems. Category III is an extension of Category II, featuring a larger band gap between OGBs**2** and the intrinsic conduction bands. Typical materials in this category include $Cs_2Sn_{0.75}Y_{0.25}Cl_6$ (Y = As, Sb, Bi). Figure S64 sand Table S3 (Supporting Information) provide an overview of this information for easy comparison. By introducing in-gap bands and out-gap bands in Category II/III materials, we can overcome inversion symmetry-induced parity-forbidden transitions, resulting in efficient electronic transitions and enhanced light emission. These insights are valuable for tuning light emission wavelengths and guiding future research in this direction.

We have explored the effect of SOC on electronic properties and light emission in our study, as SOC can bring a smaller splitting and may alter the order of bands and the allowed characteristics of transitions.[5f,26] Figures S2–S5 and S15–S62 (Supporting Information) demonstrate that the band structures and electronic transitions of Category I materials are largely unaffected by SOC, similar to the intrinsic Cs_2XCl_6. Furthermore, in the case of Category II/III materials, the predominant effect of SOC is the introduction of non-degeneracy of in-gap bands and out-gap bands, potentially leading to a shift in the corresponding energy band positions. Consequently, SOC cannot be directly disregarded in such substituted systems. However, it is important to emphasize that our primary concern in this study is the identification of qualitative trends, rather than the pursuit

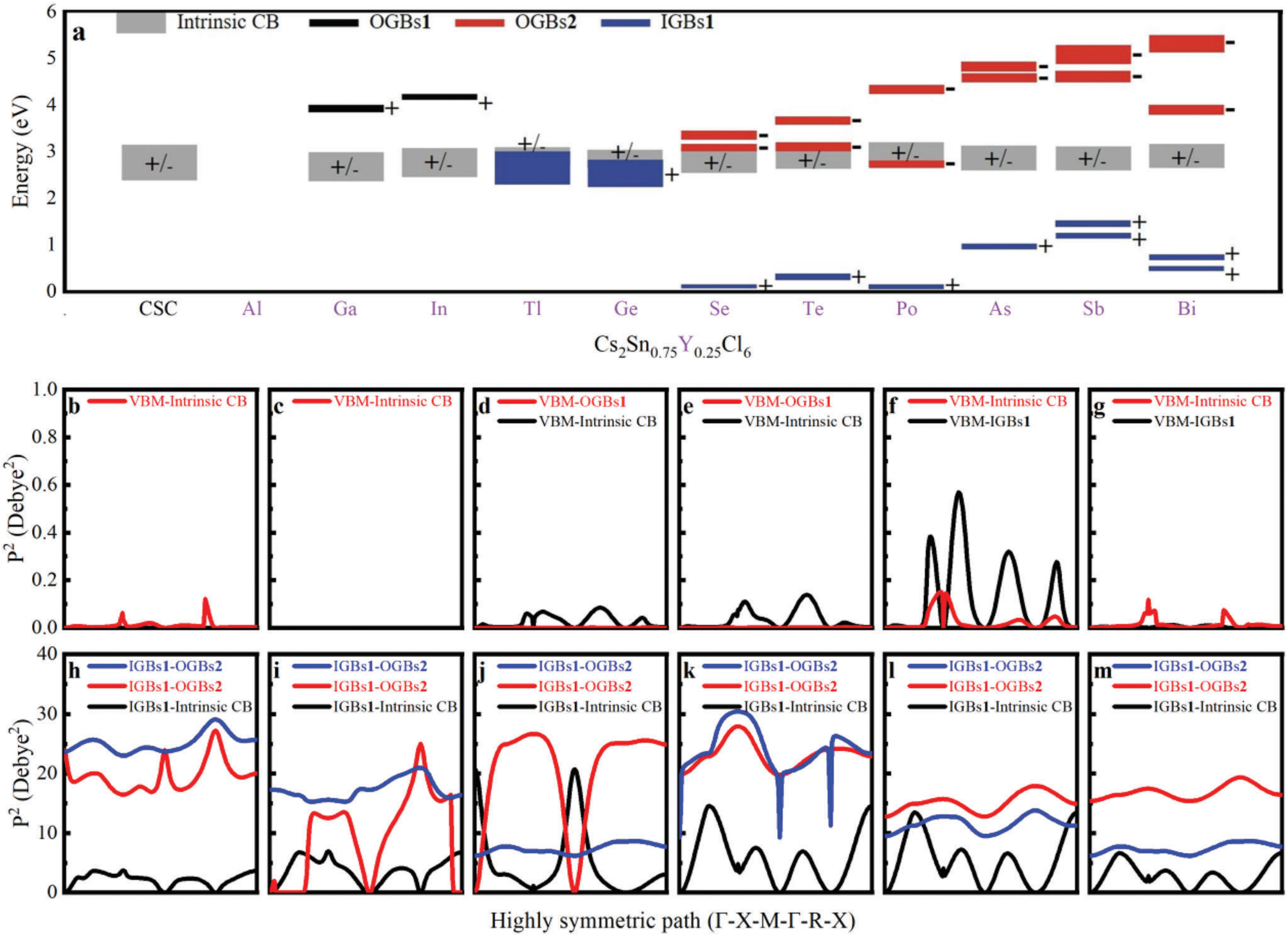

Figure 5. Impurity band and transition dipole moment. a) Approximate positions of in-gap bands (IGBs), out-gap bands (OGBs) and the intrinsic conduction bands near Fermi level with reference to the intrinsic VBM. b–m) transition dipole moments for $Cs_2Sn_{0.75}Y_{0.25}Cl_6$ (Y = Sn, Al, Ga, In, Tl, Ge, Se, Te, Po, As, Sb, Bi). The SOC is taken into account. $Cs_2Sn_{0.75}Al_{0.25}Cl_6$ lacks data due to non convergence after considering SOC, and the results without SOC can be seen in Figure S15 (Supporting Information).

of quantitative determinations. Interestingly, the outcomes with and without SOC exhibit a similar qualitative trend, signifying the continued utility of results computed without SOC. For instance, focusing on Te-substituted Cs_2SnCl_6 with a formula of $Cs_2Sn_{0.75}Te_{0.25}Cl_6$ (as depicted in Figure S25, Supporting Information), the conclusion that the transition dipole moment between in-gap bands and out-gap bands holds the most significant influence on the system remains unaffected by the inclusion of SOC. To elaborate further, let us take the transition at the high symmetry point Γ as an illustration. The transition dipole moment between the first in-gap band (band 144) and the first intrinsic conduction band (band 145) at Γ point is zero due to parity-forbidden rule. On the other hand, the transition dipole moment between in-gap band 144 and out-gap bands 148, 149, 150 at Γ point is enhanced to ≈30 Debye^2. With the incorporation of SOC, the transition dipole moment of the former remains at zero, while the latter continues to exhibit a substantial enhancement, albeit with a reduced magnitude of ≈20 Debye^2. Therefore, whether SOC is taken into consideration or not, the transition between in-gap bands and out-gap bands holds a pivotal role in augmenting electronic transitions and light emission in these substituted perovskite materials. Furthermore, we have observed within heavy atom-substituted systems (Figures S17, S18, S22–S25, S28, S29, S33–S35, S37, S40, S41, S45–S47, S49, S52, S53, S57–S59, S62, Supporting Information) that while the non-degenerate splitting induced by SOC results in notable shift of energy band position, the enhancement of transition dipole moments remains at a comparable level. These observations imply that these non-degenerate bands might uphold their parity properties even after non-degenerate splitting, aligning with findings by Meng et al.[27] In conclusion, while SOC indeed holds a significant impact on the degeneracy of bands and the magnitude of transition dipole moment, it does not alter our evaluation of the core trend.

In summary, we have found the relatively isolated nature of in-gap bands/out-gap bands in Cs_2XCl_6 materials through our calculations, suggesting that choosing the appropriate substituting cations can be a promising way to tune emission wavelength over a wide range, regardless of the hosting materials. As mentioned above, as in the case of substituting Sn with Te, substituting Bi for Sn also introduces in-gap bands and out-gap bands with opposite parity. Therefore, the double-substitution of Te and Bi for Sn in

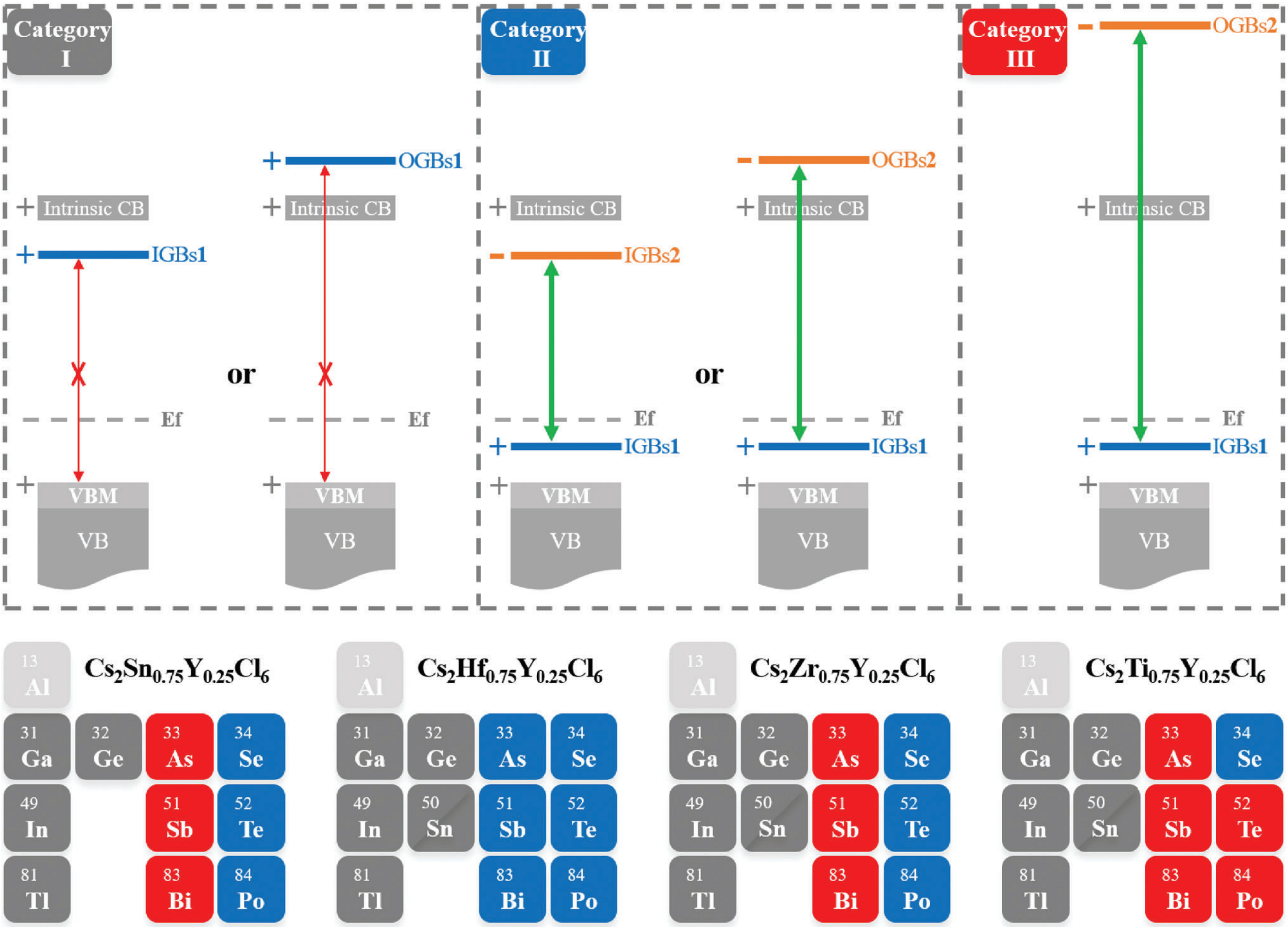
Category I
+ Intrinsic CB
+ IGBs1
Ef
+ VBM
VB
or
+ OGBs1
+ Intrinsic CB
Ef
+ VBM
VB
Category II
+ Intrinsic CB
- IGBs2
Ef
+ IGBs1
+ VBM
VB
or
- OGBs2
+ Intrinsic CB
Ef
+ IGBs1
+ VBM
VB
Category III
- OGBs2
+ Intrinsic CB
Ef
+ IGBs1
+ VBM
VB
Cs2Sn0.75Y0.25Cl6
Cs2Hf0.75Y0.25Cl6
Cs2Zr0.75Y0.25Cl6
Cs2Ti0.75Y0.25Cl6
13 Al
31 Ga
32 Ge
33 As
34 Se
49 In
50 Sn
51 Sb
52 Te
81 Tl
83 Bi
84 Po

Figure 6. Three categories of materials with different in-gap bands (IGBs)/out-gap bands (OGBs). Red cross and arrow indicate the forbidden transitions. Conversely, green arrows indicate the allowed transitions. The smaller symbol “-” near the intrinsic CB means that only a small part of conduction bands exhibits odd-parity.

Cs_2SnCl_6 may have a synergistic effect, and further exploration of this possibility is desired.

2.4. Bi and Te Double-Substituted Cs_2SnCl_6

Based on our previous discussion, it can be concluded that in-gap bands/out-gap bands in Te-monosubstituted Cs_2SnCl_6, as well as Bi-monosubstituted Cs_2SnCl_6, display an isolated nature, which is expected to persist in multi-substituted Cs_2SnCl_6 materials. To validate our findings, we have taken the Te and Bi double-substituted Cs_2SnCl_6 system as a model to perform further investigation. Through the analysis of band structures and parity properties (as shown in Figure 7a–c and Figure S65, Supporting Information), we confirmed that the positions and state compositions of in-gap bands and out-gap bands in the model system remain well-preserved. This aligns with our experimental observations of independent yellow (580 nm) and blue (450 nm) emissions generated by Te and Bi co-substituted Cs_2SnCl_6 materials (see Figure 7d), as well as the experiment conducted by Zhang et al.[12a] Reconstituted bands may facilitate the energy transfer between these distinct centers, and different substitution concentrations may lead to varying dipole matrix amplitudes and emission intensities. Thus, fine-tuning the composition ratio of substitution components in these perovskites may achieve a customizable range of white light emission, varying from warm white to pure white (see Figure 7e), while ensuring remarkable color stability over time (see Figure 7f) and durability under varying temperature conditions (see Figure 7g). In light of these findings, we have demonstrated $Cs_2Sn_{1-y}Te_yCl_6{:}n\mathrm{Bi}$ materials can serve as viable alternatives for the development of white-light-emitting diodes (WLEDs).

3. Conclusion

In summary, our study on the B-site cation substitution effect in Cs_2XCl_6 (X = Sn, Hf, Zr, Ti) using first-principles calculations has revealed that introducing in-gap bands/out-gap bands in $Cs_2X_{1-y}Y_yCl_6$ (X = Sn, Hf, Zr, Ti; Y = Se, Te, Po, As, Sb, Bi) can be a promising strategy to enhance luminescence and adjusting light emission wavelengths. We selected Te-monosubstituted Cs_2SnCl_6 as a model system for experimental exploration and found that the radiative transition from out-gap bands to in-gap bands is responsible for the single emission peak centered

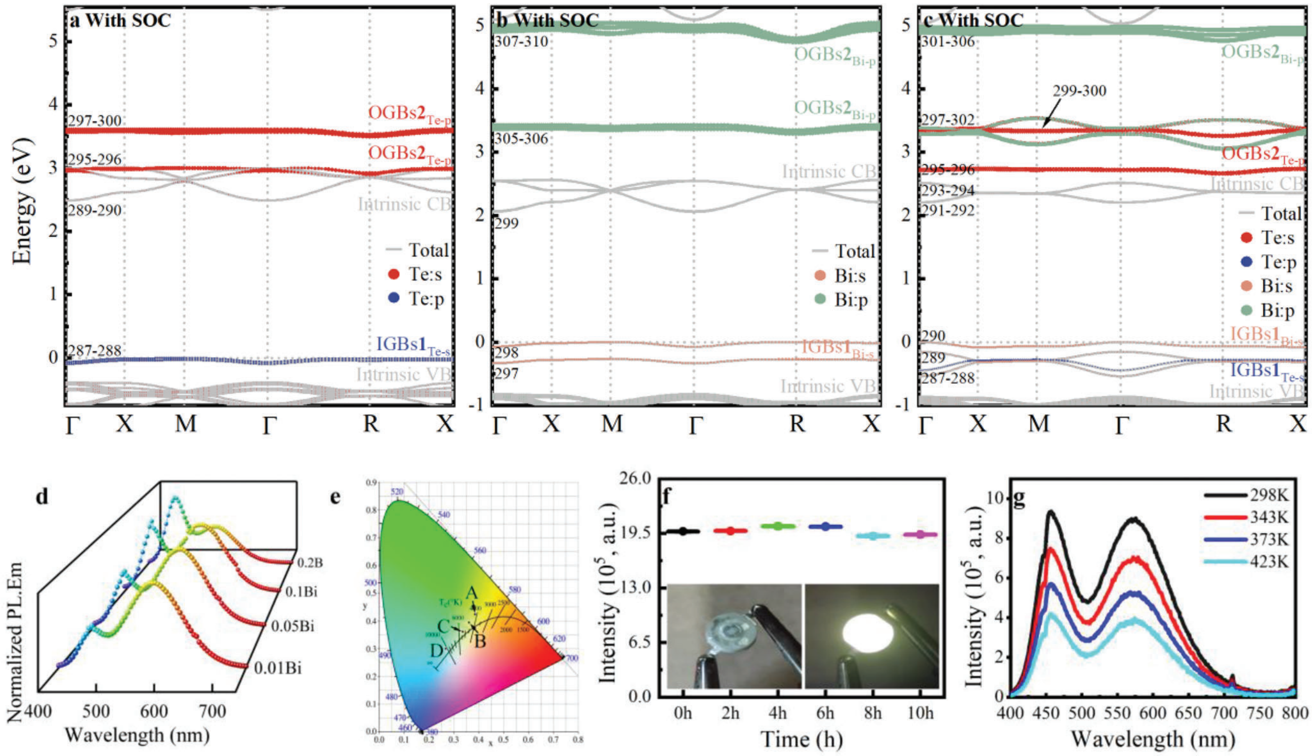

Figure 7. The electronic structure and luminescent properties of Bi and Te double-substituted Cs_2SnCl_6, and the performance characterization of the as-fabricated light-emitting diode (LED). Projected band structures with SOC for a) $Cs_2Sn_{0.75}Te_{0.25}Cl_6$, b) $Cs_2Sn_{0.75}Bi_{0.25}Cl_6$, and c) $Cs_2Sn_{0.50}Te_{0.25}Bi_{0.25}Cl_6$. The black number next to the energy band represents the band number. d) PL spectra of $Cs_2Sn_{0.70}Te_{0.30}Cl_6$:*n*Bi ($n = 0.01, 0.05, 0.10, 0.20$) powders excited at 365 nm. e) CIE coordinates of $Cs_2Sn_{0.70}Te_{0.30}Cl_6$:0.01Bi (A), $Cs_2Sn_{0.70}Te_{0.30}Cl_6$:0.05Bi (B), $Cs_2Sn_{0.70}Te_{0.30}Cl_6$:0.10Bi (C), and $Cs_2Sn_{0.70}Te_{0.30}Cl_6$:0.20Bi (D). f) Changes in light intensity of the as-fabricated LED during continuous illumination, and the insets present the working condition of the LED device. g) Temperature-dependent PL spectra of $Cs_2Sn_{0.70}Te_{0.30}Cl_6$:0.10Bi.

≈580 nm, and the broadening of the emission peak can be attributed to STE, while the Cs_2SnCl_6 phase is responsible for additional absorption/excitation peaks. Our study highlights the potential of choosing appropriate cations to regulate the position of in-gap bands/out-gap bands for fine-tuning emission wavelengths, regardless of the host materials. Moreover, the relatively isolated nature of in-gap bands/out-gap bands provide an alternative approach to achieve composite luminescence with specific requirements, as demonstrated by the tunable white-light emission achieved through the co-substitution of Te and Bi in Cs_2SnCl_6 with excellent color stability. These findings have important implications for designing and developing advanced optoelectronic devices in various fields.

4. Experimental Section

Parameters of First-Principles Calculations: The calculations were performed based on density functional theory (DFT) and projector augmented wave (PAW)[28] potential, and they were implemented in the Vienna Ab initio Simulation Package (VASP).[29] The exchange-correlation energy was treated using the generalized gradient approximation (GGA) parameterized by Perdew-Burke-Ernzerhof (PBE)[30] functional, or the meta-GGA parameterized by strongly constrained and appropriately normed (SCAN)[31] semilocal density functional. Wave functions were expanded in a plane-wave basis of 500 eV kinetic energy cut-off. Lattice constants and atomic positions were fully relaxed with a force convergence criterion of 0.01 eV Å^{-1} and an electron self-consistent convergence criterion of 1×10^{-7} eV. Brillouin-zone integration was performed by 5×5×5 gamma point-centered Monkhorst-Pack[32] grid for relaxations, standard self-consistent calculations, and PDOS. SOC was considered in some calculations with reduced accuracy. They were reflected in the reductions of the electron convergence criterion to 1×10^{-4} eV, and the Monkhorst-Pack grid to 2×2×2. Partial Band structures and band gap errors were corrected by employing the Heyd–Scuseria–Ernzerhof (HSE06) hybrid density functional, which includes 25% exact nonlocal Hartree–Fock exchange and 75% semi-local PBE exchange.[33]

Gibbs Free Energy: Gibbs free energy δG was used to evaluate the stability of materials, which was defined as,[34]

$$\delta G = E_{per} - \sum \chi_i \mu_i \tag{2}$$

where E_{per} was the cohesive energy per atom of the system studied. The χ_i was the molar fraction of composition i, satisfying the relation $\sum \chi_i = 1$. The μ_i was the chemical potential of constituent i. In this work, the binding energy per atom of Cl_2 molecule was chosen as μ_{Cl}. These μ_i (i = Cs, Sn, Hf, Zr, Ti, Al, Ga, In, Tl, Ge, As, Sb, Bi, Se, Te, Po) were selected as the cohesive energies per atom of the corresponding elementary substance.

Transition Dipole Moment and Parity: To characterize the possibility of electronic transition and light emission, Transition dipole moment associated with the transition between two states was adopted. Its calculation was an important part of excited state calculation, and it can be obtained with the following relationship,[35]

$$P_{a\to b} = \langle \varphi_b | r | \varphi_a \rangle = \frac{i\hbar}{(E_b - E_a)m} \langle \varphi_b | p | \varphi_a \rangle = \frac{i\hbar}{(E_b - E_a)} \sum_i C_{ai} C_{bi} G_i \tag{3}$$

where *a* (*b*) was the energy eigenstate with energy E_a (E_b). The plane-wave coefficients and the reciprocal space vectors with the same *k* vector were labeled C_a、C_b and *G*, respectively. The transition probability between an initial state *a* and a final state *b* was revealed by the calculated sum of the squares of transition dipole moment.[17a,27] Herein, its calculation was implemented by a command-line program VASPKIT.[35] In addition, in view of the connection between transition dipole moment and parity, parity calculations have also been performed. The parity analysis was conducted using the results obtained from Quantum Espresso and IrRep.[36]

Excited State Calculations: Following the Franck-Condon principle, exciton properties were calculated using the Δself-consistent field (DeltaSCF or ΔSCF) method,[37] in which a 2×2×2 supercell containing 288 atoms and a single gamma point were employed to avoid incorrect non-physical occupation of the band edge. To obtain an excited state, a single electron was first moved from band-edge valence band states to the band-edge conduction band states, and the corresponding structure was fully relaxed while keeping the occupancy unchanged.[38] SCAN meta-GGA[31] calculations were employed to obtain the equilibrium geometric configurations for the ground state and the excited state.

Synthesis of Samples: $Cs_2Sn_{1-y}Te_yCl_6$ and $Cs_2Sn_{1-y}Te_yCl_6$:*n*Bi solid-solution materials were synthesized by solvothermal method.[12b] For example, as for $Cs_2Sn_{1-y}Te_yCl_6$:*n*Bi, a 15-mL Teflon autoclave was soaked in nitric acid for 3 h, and then washed with deionized water for 10 min. Subsequently, CsCl (2 mmol), TeO_2 (*y* mmol), $SnCl_2$ (1-*y* mmol), and Bi_2O_3 (*n*/2 mmol) were dissolved together in the Teflon autoclave with hydrochloric acid (HCl, 5 mL, 37 wt%) solution. Next, the Teflon autoclave was put into a muffle furnace and heated continuously at 453 K for 8 h. Then, the autoclave furnace was cooled naturally to room temperature. Finally, the as-synthesized $Cs_2Sn_{1-y}Te_yCl_6$:*n*Bi crystals were obtained by immediate filtration and washed 3 times with methanol.

Measurement and Characterization: The actual chemical compositions of powder samples dissolved in HCl were determined by inductively coupled plasma optical emission spectrometry (ICP-OES)[39] operating on iCAP 7400. X-ray diffraction patterns were obtained using a Bruker D8 Advance diffractometer, wherein Cu Ka radiation was used at voltage 40 kV and current 40 mA in the range of 10°–80° (2*θ*), and its scanning rate was fixed at $4° min^{-1}$. Crystalline behaviors and energy dispersive spectrometry elemental mappings were collected by scanning electron microscopy (SEM) (Zeiss Gemini 300). Room temperature PL spectra were measured by SmartFluo-QY at ≈397 K, and temperature-dependent integrated PL spectra were measured by FLS980 equipped with xenon lamp and temperature controller system. An integrating sphere was served to test PLQY. To characterize the optical absorption properties, UV–vis absorption spectrum measurements were conducted by placing as-synthetized compounds on the reference sample substrate (high-purity $BaSO_4$). Tauc plot method[40] was used to calculate optical band gap, and the corresponding formula was as follows:

$$(\alpha h\nu)^{1/n} = A\left(h\nu - E_g\right) \tag{4}$$

where α, h, ν, A and E_g were absorption coefficient, Planck constant, incident photon frequency, constant, and band gap, respectively. And *n* depends on the type of band gap, it was equal to 0.5 for direct-gap semiconductor and 2 for indirect-gap semiconductor. The fitting between the FWHM of emission peak and temperature fitted by the following formula:[41]

$$\mathrm{FWHM}\ (\mathrm{T}) = 2.36\sqrt{S}\hbar\omega_{\mathrm{phonon}}\sqrt{\coth\left(\frac{\hbar\omega_{\mathrm{phonon}}}{2k_{\mathrm{B}}\mathrm{T}}\right)} \tag{5}$$

where *S*, $\hbar\omega_{\mathrm{phonon}}$ and k_B were Huang-Rhys factor, phonon frequency and Boltzmann constant, respectively. Among them, *S* reflects the electron phonon coupling strength.

Fabrication of LED Devices: WLED device was constructed by coupling the as-synthesized $Cs_2Sn_{0.70}Te_{0.30}Cl_6$:0.10Bi on the 365 nm LED chip. Specifically, 0.1 g $Cs_2Sn_{0.70}Te_{0.30}Cl_6$:0.10Bi powders blended with 10 g silicone gel A/B were directly painted on the surface of 365 nm LED chip, which can simplify the fabrication of WLED devices.

Supporting Information

Supporting Information is available from the Wiley Online Library or from the author.

Acknowledgements

Z.R.G. and X.S. contributed equally to this work. This work was financially supported by Hunan Provincial Natural Science Foundation of China (2021JJ30686, 2023JJ40621), the Science and Technology Innovation Program of Hunan Province (2021RC2086), the China Postdoctoral Science Foundation (2022M722665), and the Postgraduate Scientific Research Innovation Project of Hunan Province (CX20210621).

Conflict of Interest

The author declare no conflict of interest.

Data Availability Statement

The data that support the findings of this study are available from the corresponding author upon reasonable request.

Keywords

composition segregation, in/out-gap bands, lead-free halide perovskites, luminescence tailoring, tunable white-light emission

Received: April 24, 2023
Revised: August 14, 2023
Published online: September 10, 2023

---

[1] a) D. Chen, Y. Liu, C. Yang, J. Zhong, S. Zhou, J. Chen, H. Huang, *Nanoscale* **2019**, *11*, 17216; b) J. Shamsi, A. S. Urban, M. Imran, L. De Trizio, L. Manna, *Chem. Rev.* **2019**, *119*, 3296; c) Y. Rong, Y. Hu, A. Mei, H. Tan, M. I. Saidaminov, S. I. Seok, M. D. McGehee, E. H. Sargent, H. Han, *Science* **2018**, *361*, eaat8235; d) G. Yang, Z. Ni, Z. J. Yu, B. W. Larson, Z. Yu, B. Chen, A. Alasfour, X. Xiao, J. M. Luther, Z. C. Holman, J. Huang, *Nat. Photonics* **2022**, *16*, 588; e) T.-H. Han, K. Y. Jang, Y. Dong, R. H. Friend, E. H. Sargent, T.-W. Lee, *Nat. Rev. Mater.* **2022**, *7*, 757.

[2] a) H. Cho, S.-H. Jeong, M.-H. Park, Y.-H. Kim, C. Wolf, C.-L. Lee, J. H. Heo, A. Sadhanala, N. Myoung, S. Yoo, S. H. Im, R. H. Friend, T.-W. Lee, *Science* **2015**, *350*, 1222; b) Z. Xiao, R. A. Kerner, L. Zhao, N. L. Tran, K. M. Lee, T.-W. Koh, G. D. Scholes, B. P. Rand, *Nat. Photonics* **2017**, *11*, 108; c) H.-K. Seo, H. Kim, J. Lee, M.-H. Park, S.-H. Jeong, Y.-H. Kim, S.-J. Kwon, T.-H. Han, S. Yoo, T.-W. Lee, *Adv. Mater.* **2017**, *29*, 1605587; d) A. H. Slavney, R. W. Smaha, I. C. Smith, A. Jaffe, D. Umeyama, H. I. Karunadasa, *Inorg. Chem.* **2017**, *56*, 46; e) L. Kong, X. Zhang, C. Zhang, L. Wang, S. Wang, F. Cao, D. Zhao, A. L. Rogach, X. Yang, *Adv. Mater.* **2022**, *34*, 2205217.

[3] a) T. Krishnamoorthy, H. Ding, C. Yan, W. L. Leong, T. Baikie, Z. Zhang, M. Sherburne, S. Li, M. Asta, N. Mathews, S. G. Mhaisalkar, *J. Mater. Chem. A* **2015**, *3*, 23829; b) B. Chabot, E. Parthé, *Acta Crystallogr. B* **1978**, *34*, 645; c) A. J. Lehner, D. H. Fabini, H. A. Evans, C.-A.

Hébert, S. R. Smock, J. Hu, H. Wang, J. W. Zwanziger, M. L. Chabinyc, R. Seshadri, *Chem. Mater.* **2015**, *27*, 7137; d) J. Sun, J. Yang, J. I. Lee, J. H. Cho, M. S. Kang, *J. Phys. Chem. Lett.* **2018**, *9*, 1573; e) M. Leng, Z. Chen, Y. Yang, Z. Li, K. Zeng, K. Li, G. Niu, Y. He, Q. Zhou, J. Tang, *Angew. Chem., Int. Ed.* **2016**, *55*, 15012; f) T. Zhu, Y. Yang, X. Gong, *ACS Appl. Mater. Interfaces* **2020**, *12*, 26776.

[4] a) Q. Zhang, S. Liu, M. He, W. Zheng, Q. Wan, M. Liu, X. Liao, W. Zhan, C. Yuan, J. Liu, H. Xie, X. Guo, L. Kong, L. Li, *Angew. Chem., Int. Ed.* **2022**, *61*, e202205463; b) T. C. Jellicoe, J. M. Richter, H. F. J. Glass, M. Tabachnyk, R. Brady, S. E. Dutton, A. Rao, R. H. Friend, D. Credgington, N. C. Greenham, M. L. Böhm, *J. Am. Chem. Soc.* **2016**, *138*, 2941; c) C. Kang, H. Rao, Y. Fang, J. Zeng, Z. Pan, X. Zhong, *Angew. Chem., Int. Ed.* **2021**, *60*, 660.

[5] a) A. E. Fedorovskiy, N. A. Drigo, M. K. Nazeeruddin, *Small Methods* **2020**, *4*, 1900426; b) S. Aslam, A. S. Farooqi, M. Y. A. Rahman, S. A. M. Samsuri, *Phys. Status Solidi A* **2022**, *219*, 2100671; c) M. Talebi, A. Mokhtari, V. Soleimanian, *J. Phys. Chem. Solids* **2023**, *176*, 111262; d) A. E. Maughan, A. M. Ganose, M. M. Bordelon, E. M. Miller, D. O. Scanlon, J. R. Neilson, *J. Am. Chem. Soc.* **2016**, *138*, 8453; e) M. Jin, W. Zheng, Z. Gong, P. Huang, R. Li, J. Xu, X. Cheng, W. Zhang, X. Chen, *Nano Res.* **2022**, *15*, 6422; f) S. R. Kavanagh, C. N. Savory, S. M. Liga, G. Konstantatos, A. Walsh, D. O. Scanlon, *J. Phys. Chem. Lett.* **2022**, *13*, 10965; g) W. Rahim, A. Cheng, C. Lyu, T. Shi, Z. Wang, D. O. Scanlon, R. G. Palgrave, *Chem. Mater.* **2020**, *32*, 9573.

[6] a) Z. Tan, Y. Chu, J. Chen, J. Li, G. Ji, G. Niu, L. Gao, Z. Xiao, J. Tang, *Adv. Mater.* **2020**, *32*, 2002443; b) D. Chen, X. Zhang, J. Wei, L. Zhou, P. Chen, Q. Pang, J. Z. Zhang, *Inorg. Chem. Front.* **2022**, *9*, 4695; c) H. Yin, J. Chen, P. Guan, D. Zheng, Q. Kong, S. Yang, P. Zhou, B. Yang, T. Pullerits, K. Han, *Angew. Chem., Int. Ed.* **2021**, *60*, 22693; d) J. Li, Z. Tan, M. Hu, C. Chen, J. Luo, S. Li, L. Gao, Z. Xiao, G. Niu, J. Tang, *Front. Optoelectron.* **2019**, *12*, 352; e) R. Zeng, K. Bai, Q. Wei, T. Chang, J. Yan, B. Ke, J. Huang, L. Wang, W. Zhou, S. Cao, J. Zhao, B. Zou, *Nano Res.* **2021**, *14*, 1551.

[7] a) Z. F. Tan, J. H. Li, C. Zhang, Z. Li, Q. S. Hu, Z. W. Xiao, T. Kamiya, H. Hosono, G. D. Niu, E. Lifshitz, Y. B. Cheng, J. Tang, *Adv. Funct. Mater.* **2018**, *28*, 1801131; b) A. M. Ganose, C. N. Savory, D. O. Scanlon, *J. Phys. Chem. Lett.* **2015**, *6*, 4594; c) T. Shi, W.-J. Yin, F. Hong, K. Zhu, Y. Yan, *Appl. Phys. Lett.* **2015**, *106*, 103902; d) J. Kang, L.-W. Wang, *J. Phys. Chem. Lett.* **2017**, *8*, 489; e) Z. Xiao, K. Z. Du, W. Meng, D. B. Mitzi, Y. Yan, *Angew. Chem., Int. Ed.* **2017**, *56*, 12107.

[8] a) A. Kaltzoglou, M. Antoniadou, A. G. Kontos, C. C. Stoumpos, D. Perganti, E. Siranidi, V. Raptis, K. Trohidou, V. Psycharis, M. G. Kanatzidis, P. Falaras, *J. Phys. Chem. C* **2016**, *120*, 11777; b) H. Zhang, L. Zhu, J. Cheng, L. Chen, C. Liu, S. Yuan, *Materials* **2019**, *12*, 1501.

[9] a) A. Burger, E. Rowe, M. Groza, K. M. Figueroa, N. J. Cherepy, P. R. Beck, S. Hunter, S. A. Payne, *Appl. Phys. Lett.* **2015**, *107*, 143505; b) K. Saeki, Y. Fujimoto, M. Koshimizu, T. Yanagida, K. Asai, *Appl. Phys. Express* **2016**, *9*, 042602; c) P. S. Bryan, S. A. Ferranti, *J. Lumin.* **1984**, *31–32*, 117; d) B. Kang, K. Biswas, *J. Phys. Chem. C* **2016**, *120*, 12187.

[10] a) F. Zhang, Y. Zhou, Z. Chen, X. Niu, H. Wang, M. Jia, J. Xiao, X. Chen, D. Wu, X. Li, Z. Shi, C. Shan, *Laser Photonics Rev.* **2023**, *17*, 2200848; b) S. Nagorny, *Physics* **2021**, *3*, 320; c) S. Liu, B. Yang, J. Chen, D. Wei, D. Zheng, Q. Kong, W. Deng, K. Han, *Angew. Chem., Int. Ed.* **2020**, *59*, 21925; d) A. Veronese, M. Patrini, D. Bajoni, C. Ciarrocchi, P. Quadrelli, L. Malavasi, *Front. Chem.* **2020**, *8*; e) S. Liu, B. Yang, J. Chen, D. Zheng, Z. Tang, W. Deng, K. Han, *Laser Photonics Rev.* **2022**, *16*, 2100439; f) T.-W. Lin, C. Su, C. C. Lin, *J. Inform. Display* **2019**, *20*, 209.

[11] a) C. Cardenas, A. Burger, M. L. DiVacri, B. Goodwin, M. Groza, M. Laubenstein, S. Nagorny, S. Nisi, E. Rowe, *Nucl. Instrum. Methods Phys. Res.* **2017**, *872*, 23; b) C. Cardenas, A. Burger, B. Goodwin, M. Groza, M. Laubenstein, S. Nagorny, E. Rowe, *Nucl. Instrum. Methods Phys. Res.* **2017**, *869*, 63; c) E. Ariesanti, R. Hawrami, A. Burger, S. Motakef, *J. Lumin.* **2020**, *217*, 116784; d) R. Hawrami, E. Ariesanti, V. Buliga, L. Matei, S. Motakef, A. Burger, *J. Cryst. Growth* **2020**, *533*, 125473; e) C. Delzer, M. Zhuravleva, L. Stand, C. Melcher, N. Cherepy, S. Payne, R. Sanner, J. P. Hayward, *J. Cryst. Growth* **2020**, *531*, 125336.

[12] a) W. Zhang, W. Zheng, L. Li, P. Huang, Z. Gong, Z. Zhou, J. Sun, Y. Yu, X. Chen, *Angew. Chem., Int. Ed.* **2022**, *61*, e202116085; b) L. Zi, W. Xu, Z. Song, R. Sun, S. Liu, T. Xie, J. Zhu, S. Lu, H. Song, *J. Mater. Chem. C* **2023**, *11*, 2695; c) J. Sun, W. Zheng, P. Huang, M. Zhang, W. Zhang, Z. Deng, S. Yu, M. Jin, X. Chen, *Angew. Chem., Int. Ed.* **2022**, *61*, e202201993.

[13] X. Wang, W. Meng, W. Liao, J. Wang, R. G. Xiong, Y. Yan, *J. Phys. Chem. Lett.* **2019**, *10*, 501.

[14] a) Y. Zhou, T. Fang, G. Liu, H. Xiang, L. Yang, Y. Li, R. Wang, D. Yan, Y. Dong, B. Cai, H. Zeng, *Adv. Funct. Mater.* **2021**, *31*, 2106871; b) Z. Gong, W. Zheng, Y. Gao, P. Huang, D. Tu, R. Li, J. Wei, W. Zhang, Y. Zhang, X. Chen, *Angew. Chem., Int. Ed.* **2019**, *58*, 6943.

[15] a) L. Zhao, X. Chen, J. Fu, C. Xue, M. Zhang, W. Wen, J. Wu, *Appl. Surf. Sci.* **2021**, *567*, 150827; b) J. Jiang, S. Chen, C. Zhao, C. Lin, X. Wu, M. Gao, T. Lin, C. Fang, *J. Am. Chem. Soc.* **2023**, *106*, 913; c) L. Wang, Y. Xiao, *J. Alloy. Compd.* **2022**, *902*, 163797.

[16] a) L. Zhou, J.-F. Liao, Z.-G. Huang, X.-D. Wang, Y.-F. Xu, H.-Y. Chen, D.-B. Kuang, C.-Y. Su, *ACS Energy Lett.* **2018**, *3*, 2613; b) M. Faizan, K. C. Bhamu, G. Murtaza, X. He, N. Kulhari, M. M. Al-Anazy, S. H. Khan, *Sci. Rep.* **2021**, *11*, 6965; c) Y. Cai, W. Xie, H. Ding, Y. Chen, K. Thirumal, L. H. Wong, N. Mathews, S. G. Mhaisalkar, M. Sherburne, M. Asta, *Chem. Mater.* **2017**, *29*, 7740.

[17] a) J. Luo, X. Wang, S. Li, J. Liu, Y. Guo, G. Niu, L. Yao, Y. Fu, L. Gao, Q. Dong, C. Zhao, M. Leng, F. Ma, W. Liang, L. Wang, S. Jin, J. Han, L. Zhang, J. Etheridge, J. Wang, Y. Yan, E. H. Sargent, J. Tang, *Nature* **2018**, *563*, 541; b) B. Chen, Y. Guo, Y. Wang, Z. Liu, Q. Wei, S. Wang, A. L. Rogach, G. Xing, P. Shi, F. Wang, *J. Am. Chem. Soc.* **2021**, *143*, 17599.

[18] J. Jiang, G. Niu, L. Sui, X. Wang, X. Zeng, Y. Zhang, L. Che, G. Wu, K. Yuan, X. Yang, *Adv. Opt. Mater.* **2022**, *11*, 2202634.

[19] a) R. I. Eglitis, E. A. Kotomin, V. A. Trepakov, S. E. Kapphan, G. Borstel, *J. Phys.: Condens. Matter* **2002**, *14*, L647; b) E. A. Kotomin, R. I. Eglitis, G. Borstel, *J. Phys.: Condens. Matter* **2000**, *12*, L557; c) B. Kang, K. Biswas, *J. Phys. Chem. Lett.* **2018**, *9*, 830; d) M. L. Crespillo, J. T. Graham, F. Agulló-López, Y. Zhang, W. J. Weber, *Crystals* **2019**, *9*, 95.

[20] T. Hu, M. D. Smith, E. R. Dohner, M.-J. Sher, X. Wu, M. T. Trinh, A. Fisher, J. Corbett, X. Y. Zhu, H. I. Karunadasa, A. M. Lindenberg, *J. Phys. Chem. Lett.* **2016**, *7*, 2258.

[21] a) F. Zhang, Z. Zhao, B. Chen, H. Zheng, L. Huang, Y. Liu, Y. Wang, A. L. Rogach, *Adv. Opt. Mater.* **2020**, *8*, 1901723; b) K. M. McCall, C. C. Stoumpos, O. Y. Kontsevoi, G. C. B. Alexander, B. W. Wessels, M. G. Kanatzidis, *Chem. Mater.* **2019**, *31*, 2644.

[22] F. Zhang, Y. Zhou, Z. Chen, M. Wang, Z. Ma, X. Chen, M. Jia, D. Wu, J. Xiao, X. Li, Y. Zhang, Z. Shi, C. Shan, *Adv. Mater.* **2022**, *34*, 2204801.

[23] a) Y.-K. Jung, S. Kim, Y. C. Kim, A. Walsh, *J. Phys. Chem. Lett.* **2021**, *12*, 8447; b) R. Gautier, M. Paris, F. Massuyeau, *J. Am. Chem. Soc.* **2019**, *141*, 12619; c) S. Kahmann, E. K. Tekelenburg, H. Duim, M. E. Kamminga, M. A. Loi, *Nat. Commun.* **2020**, *11*, 2344; d) Q. Li, Z. Chen, B. Yang, L. Tan, B. Xu, J. Han, Y. Zhao, J. Tang, Z. Quan, *J. Am. Chem. Soc.* **2020**, *142*, 1786.

[24] W. Tao, C. Zhang, Q. Zhou, Y. Zhao, H. Zhu, *Nat. Commun.* **2021**, *12*, 1400.

[25] W. Yang, P. Dang, G. Zhang, H. Lian, G. Li, J. Lin, *Inorg. Chem.* **2022**, *61*, 5903.

[26] a) B. Cucco, G. Bouder, L. Pedesseau, C. Katan, J. Even, M. Kepenekian, G. Volonakis, *Appl. Phys. Lett.* **2021**, *119*, 181903; b) B. Cucco, C. Katan, J. Even, M. Kepenekian, G. Volonakis, *ACS Mater. Lett.* **2023**, *5*, 52.

[27] W. Meng, X. Wang, Z. Xiao, J. Wang, D. B. Mitzi, Y. Yan, *J. Phys. Chem. Lett.* **2017**, *8*, 2999.

[28] a) P. E. Blochl, *Phys. Rev. B* **1994**, *50*, 17953; b) G. Kresse, D. Joubert, *Phys. Rev. B* **1999**, *59*, 1758.

[29] a) G. Kresse, J. Furthmüller, *Comp. Mater. Sci.* **1996**, *6*, 15; b) G. Kresse, J. Furthmuller, *Phys. Rev. B* **1996**, *54*, 11169.

[30] J. P. Perdew, K. Burke, M. Ernzerhof, *Phys. Rev. Lett.* **1996**, *77*, 3865.

[31] J. Sun, A. Ruzsinszky, J. P. Perdew, *Phys. Rev. Lett.* **2015**, *115*, 036402.

[32] H. J. Monkhorst, J. D. Pack, *Phys. Rev. B* **1976**, *13*, 5188.

[33] A. V. Krukau, O. A. Vydrov, A. F. Izmaylov, G. E. Scuseria, *J. Chem. Phys.* **2006**, *125*, 224106.

[34] W. Zou, Z. Z. Yu, C. X. Zhang, J. X. Zhong, L. Z. Sun, *Appl. Phys. Lett.* **2012**, *100*, 103109.

[35] V. Wang, N. Xu, J.-C. Liu, G. Tang, W.-T. Geng, *Comput. Phys. Commun.* **2021**, *267*, 108033.

[36] a) M. Iraola, J. L. Mañes, B. Bradlyn, M. K. Horton, T. Neupert, M. G. Vergniory, S. S. Tsirkin, *Comput. Phys. Commun.* **2022**, *272*, 108226; b) L. Elcoro, B. Bradlyn, Z. Wang, M. G. Vergniory, J. Cano, C. Felser, B. A. Bernevig, D. Orobengoa, G. de la Flor, M. I. Aroyo, *J. Appl. Crystallogr.* **2017**, *50*, 1457.

[37] A. Hellman, B. Razaznejad, B. I. Lundqvist, *J. Chem. Phys.* **2004**, *120*, 4593.

[38] P. Fu, M. Huang, Y. Shang, N. Yu, H.-L. Zhou, Y.-B. Zhang, S. Chen, J. Gong, Z. Ning, *ACS Appl. Mater. Interfaces* **2018**, *10*, 34363.

[39] A. Ayar, D. Sert, N. Akın, *Environ. Monit. Assess.* **2009**, *152*, 1.

[40] a) J. Tauc, R. Grigorovici, A. Vancu, *Phys. Status Solidi B* **1966**, *15*, 627; b) E. A. Davis, N. F. Mott, *Philos. Mag.* **1970**, *22*, 0903.

[41] W. Stadler, D. M. Hofmann, H. C. Alt, T. Muschik, B. K. Meyer, E. Weigel, G. Müller-Vogt, M. Salk, E. Rupp, K. W. Benz, *Phys. Rev. B* **1995**, *51*, 10619.